Average Energy Transfer Characteristics and Control Strategy of Active Feedback Sound Insulation for Water-Filled Acoustic System Based on Double-Layer Plate Structure

Likang Wang [1,2]**, Rui Huo** [1,2,]*****, Shuqing Liu** [1,2]**, Yuanbo Li** [3] **and Dewen He** [4]

1   School of Mechanical Engineering, Shandong University, Jinan 250061, China
2   Key Laboratory of High Efficiency and Clean Mechanical Manufacture, Shandong University, Ministry of Education, Jinan 250061, China
3   No. 92143 Unit of PLA, Sanya 572000, China
4   Wulian County Yuxing Machinery Manufacturing Co., Ltd., Rizhao 262399, China
*   Correspondence: huorui@sdu.edu.cn

Abstract: The double-layer plate structure in passive sound insulation systems can improve the high-frequency sound insulation performance, but it is still not ideal in the low-frequency region. The actuator of the active sound insulation system can adjust the stiffness and damping in real time, with strong adaptability and adjustability. Therefore, in this paper, active actuators and feedback control strategy are applied to a double-layer plate structure to improve the low-frequency sound insulation performance of a water-filled acoustic cavity system. The theoretical model of a sound insulation system with a double-layer plate structure and active feedback control strategy is established for a water-filled acoustic cavity. The average energy transfer is used as an evaluation index for the active sound insulation effect of the system, and the calculation method of this index is derived. Then, the MATLAB numerical simulation is used to analyze the effect of six feedback control parameters on the average energy transfer of the system. Finally, it is concluded that when the feedback parameters are within the effective range, all six feedback control methods can produce significant effects on the low-frequency sound insulation of the system, but the effective range of some parameters is narrow.

Keywords: active sound insulation; double-layer plate structure; water-filled acoustic cavity; active feedback control; control strategy

1. Introduction

Sonar is the core equipment that people use for underwater measurement and observation, and sonar detection is currently the only effective means to achieve long-range diving in the military. The practical value and significance of enhancing sonar detection capability by reducing sonar self-noise cannot be overstated. The most commonly used means to solve the problem of noise reduction in naval structures is the application of sound insulation technology in the noise transmission path. It can be divided into two ways: passive sound insulation and active sound insulation. In the current ship design and use, the traditional passive sound insulation structure design is still commonly used. It has an excellent sound insulation effect for the high-frequency region, but the effect is not satisfactory for the low-frequency region [1–3]. Active sound insulation is a branch of active control technology [4]. The actuator of the active sound insulation system can adjust the stiffness and damping in real time, and has strong adaptability and adjustability, so it has obvious advantages in sound insulation.

In 2017, the China Shipbuilding Science Research Center (CSRC) summarized the remarkable progress made in underwater noise research on Chinese ships over the past three decades and raised several cutting-edge fundamental issues: research in sound insulation methods should be further developed from passive sound insulation to combine

active and passive sound insulation, and from single-layer sound insulation to multi-layer sound insulation; the low-frequency sound insulation performance of acoustic covering materials should be further improved, and the research of components should be developed from the basic type to the high-performance type; research on sonar self-noise should be conducted on low-frequency pressure-resistant sound insulation and sound-absorbing materials or structures [5].

In recent years, some structures are widely used in sound insulation systems, such as box sound insulation structures, cladding, laminated structures, double-layered plates, and so on [6–8]. Tang et al. [9] analytically researched the influence law of the cover layer on the vibration response of the shell and plate structural system for different stiffness, mass and damping parameters. Wang [10] researched the effect law of the design parameters of composite plates on the sound insulation system in the low-frequency region by using the Rayleigh integral method, impedance method, and modal decomposition method. Xu et al. [11] studied the effect of sound-absorbing materials and the damping of the box structure on the acoustic performance of the sound insulation device using statistical energy analysis, and demonstrated that sound-absorbing materials can effectively improve the medium- and high-frequency sound insulation performance of box sound insulation devices, but the contribution to the low- and medium-frequency regions is weak. Gao [12] studied the sound insulation performance of double-layer reinforced plates, infinite unidirectional double-cycle and orthogonal-cycle reinforced plates by comparing the vibration response results and concluded that the sound insulation effect of double-layer plates is better than that of single-layer plates. Kaidouchi et al. [13] tested several materials used in aerospace composite structures by modal and steady-state analysis and concluded that the glass fiber-reinforced polymer cores with fiber-reinforced plastic finish material have better vibro-acoustic and sound transmission characteristics.

Yang [14] took resin-based carbon fiber composite laminates as the object of study and analyzed the acoustic vibration characteristics of the acoustic system with corrugated core sandwich plate structure based on the theoretical derivation and simulation of the wave-based method. Gao et al. [15] designed Y-shaped folded sandwich plates based on the isostatic stiffness method with a 33.19% weight reduction and a 68.4% reduction in response amplitude than the conventional reinforced plates, which have a better noise reduction performance. Langfeldt et al. [16] made a significant shift in the mass–air resonance frequency of the double wall by adjusting the Helmholtz resonator to increase the energy transfer loss of the double wall using the induced resonance. Leng [17] proposed a double-layer plate structure with rubber grids for low-frequency sound insulation, and although the effect is better than that of the traditional light barrier sheet, the structure still belongs to the passive sound insulation category and cannot take into account the sound insulation effect in the resonance and high-frequency regions. Bai [18] modeled and simulated the vibration and sound radiation of a double-layer cylindrical shell system based on the impedance analysis method, and found that the solid ribbed plate has a certain effect on the sound insulation of the double-layer cylindrical shell in the medium- and high-frequency regions, and no significant effect in the frequency area below 100 Hz. Zhang et al. [19] proposed an acoustic isolation metamaterial for distributed piezoelectric resonators, derived an acoustic prediction model, and verified its correctness by the STL simulation results of the corresponding acoustic-structural fully coupled finite element model.

In recent years, many control strategies have been proposed one after another for solving low-frequency sound insulation problems in practical engineering, such as canopy damping control, active feedback control, passive control, discrete control, optimal control, and other methods [20–22]. Ma et al. [23] developed an investigation on the mechanism analysis of the active control of sound transmission through an orthogonal rib-stiffened double-panel structure, and used numerical analysis to verify the accuracy of the model. Zuo et al. [24] used the impedance analysis method to model a vibration isolation system, and introduced a feedback control link to analyze the vibration isolation performance of the active control system under different conditions. Although active control technology

is used in noise reduction in areas such as high-speed trains and automobiles [25–27], it is still not widely used. In particular, there are fewer applications in underwater sound insulation systems.

As can be seen from the above literature review, passive sound insulation structures are still mainly used with various damping sandwich layers for double-layer panel systems to solve low-frequency problems. In recent years, there has been little research on active control techniques in sound insulation applications, especially in underwater sound insulation. In this paper, the active actuator is combined with the double-layer plate structure, and the active feedback control link is added, forming an active sound insulation structure with a double-layer plate. It is applied to underwater sound insulation systems and its control strategy is analyzed. Different from the average sound pressure level commonly used in related studies, the average power flow is used as an evaluation index to analyze the sound insulation performance of the system from the perspective of energy transfer, which is more comprehensive.

In this paper, based on the theoretical model for a coupled system of elastic plate structure and water-filled acoustic cavity, the theoretical model of a sound insulation system with the double-layer plate structure and active feedback control strategy is established for the water-filled acoustic cavity. The average energy transfer of the system is derived and used as the evaluation index of the active sound insulation effect. Then, MATLAB numerical simulations are used to analyze the average energy transfer characteristics of the system under continuous variation of each feedback parameter. Finally, some important conclusions are drawn.

2. Modal Analysis and Calculation of the Average Energy Input for Each Part of the Active Feedback Sound Insulation System

Figure 1 shows the schematic of the sound insulation system with a double-layer plate structure and active actuators for the water-filled acoustic cavity. In this system, active isolation units are applied in the double-layer plate structure, where each isolation unit is a parallel of resilient support and an active actuator. The stiffness of the elastic support needs to be properly designed so that it has sufficient stiffness to maintain the stability of the system while allowing for a slight relative vibration between the upper and lower plates. The active actuator is used to provide additional control to attenuate the transfer of external excitation energy to the sound field within the chamber. Improperly increasing damping is actually detrimental to sound insulation. Therefore, controlling the variation of damping is not the only effective control strategy for active sound insulation systems. Here, an attempt is made to add an active feedback control link to the sound insulation system.
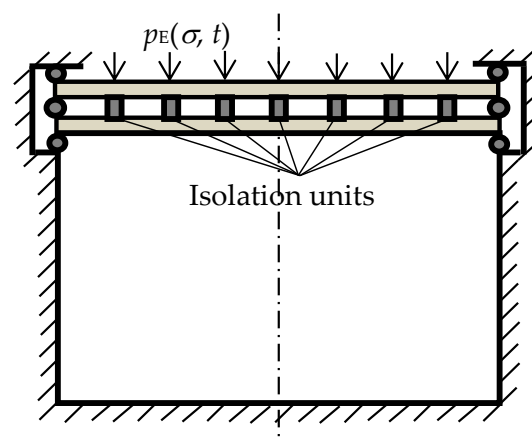
Figure 1. Schematic of the sound insulation system with double-layer plate structure and active actuators for the water-filled acoustic cavity.

2.1. Modal Analysis of Coupling Structure of the Lower Plate and the Water-Filled Chamber

The closed water-filled chamber, with V denoting the area filled with water, is a passive sound field with fluctuating equations in the coordinate system O-X-Y-Z:

$$K_0 \nabla^2 \Phi(\sigma, t) - \rho_0 \frac{\partial^2 \Phi(\sigma, t)}{\partial t^2} = 0 (\sigma \in V) \tag{1}$$

where $\nabla^2 = \partial^2/\partial x^2 + \partial^2/\partial y^2 + \partial^2/\partial z^2$; $K_0 = \rho_0 c_0^2$ is the volume stiffness of water; ρ_0 is the density of water; c_0 is the speed of sound in water; $\Phi(\sigma, t)(\sigma = (x, y, z) \in V)$ is the velocity potential function, then the medium particle vibration velocity $u(\sigma, t) = \nabla \Phi(\sigma, t)$ and the sound pressure $p(\sigma, t) = -\rho_0 \partial \Phi(\sigma, t)/\partial t$ and can be derived from $\Phi(\sigma, t)$.

Certain areas on the boundary of the water-filled chamber are rigid, denoted by D_S; certain areas are elastic, denoted by D_F. For $\sigma \in D_F$ and $\sigma \in D_S$, the boundary conditions are available, respectively:

$$\frac{\partial \Phi(\sigma, t)}{\partial n} = u_n(\sigma, t) \quad (\sigma \in D_F) \tag{2}$$

$$\frac{\partial \Phi(\sigma, t)}{\partial n} = 0 \quad (\sigma \in D_S) \tag{3}$$

where n denotes the direction normal to the boundary outside the cavity wall; $u_n(\sigma, t)$ is the normal velocity of the elastic cavity wall vibration.

If all boundaries are rigid, which means $D_F = 0$, Equation (1) has modal solutions $\Phi_{Ar}(\sigma) \cdot \exp(j\omega_{Ar}t)$, $r = 0, 1, 2, \cdots$, where ω_{Ar} is the rth order natural frequency of the cavity wall and $\Phi_{Ar}(\sigma)$ is the shape function corresponding to ω_{Ar}. Additionally, $\Phi_{Ar}(\sigma)$ has the following orthogonal properties:

$$\begin{cases} \iiint_V \frac{\Phi_{Ar}(\sigma)\Phi_{As}(\sigma)}{\rho_0 c_0^2} \mathrm{d}v = \begin{cases} 0 & r \neq s \\ M_{Ar} & r = s \end{cases} \\ \iiint_V \frac{[\nabla \Phi_{Ar}(\sigma)]^{\mathrm{T}}[\nabla \Phi_{As}(\sigma)]}{\rho_0} \mathrm{d}v = \begin{cases} 0 & r \neq s \\ \omega_{Ar}^2 M_{Ar} & r = s \end{cases} \end{cases} \tag{4}$$

where $\nabla \Phi_{Ar}(\sigma) = [\partial \Phi_{Ar}/\partial x, \partial \Phi_{Ar}/\partial y, \partial \Phi_{Ar}/\partial z]^{\mathrm{T}}$ is the column gradient vector of the shape function $\Phi_{Ar}(\sigma)$; M_{Ar} is the rth acoustic mode mass for the rigid boundary condition.

Let the solution of Equation (1) have the modal superposition form:

$$\Phi(\sigma, t) = \sum_{r=0}^{\infty} \Phi_{Ar}(\sigma) A_r(t) = [\boldsymbol{\Phi}_A(\sigma)]^{\mathrm{T}} A(t) (\sigma \in V) \tag{5}$$

where $\boldsymbol{\Phi}_A(\sigma) = [\Phi_{A0}(\sigma), \Phi_{A1}(\sigma), \Phi_{A2}(\sigma), \ldots]^{\mathrm{T}}$ and $A(t) = [A_0(t), A_1(t), A_2(t), \ldots]^{\mathrm{T}}$ are the column vectors of $\Phi_{Ar}(\sigma)$ and its corresponding modal coordinate $A_r(t)$, respectively.

Using the above equation and Equation (1), the following equation can be obtained:

$$\iiint_V \boldsymbol{\Phi}_A(\sigma) \left[\nabla^2 \Phi(\sigma, t) \right] \mathrm{d}V - \frac{1}{c_0^2} \iiint_V \left\{ \boldsymbol{\Phi}_A(\sigma) [\boldsymbol{\Phi}_A(\sigma)]^{\mathrm{T}} \ddot{A}(t) \right\} \mathrm{d}V = 0 \tag{6}$$

Applying Gauss' theorem to the first term of the above equation:

$$\frac{1}{c_0^2} \iiint_V \left\{ \boldsymbol{\Phi}_A(\sigma) [\boldsymbol{\Phi}_A(\sigma)]^{\mathrm{T}} \ddot{A}(t) \right\} \mathrm{d}V + \iiint_V [\nabla \boldsymbol{\Phi}_A(\sigma)]^{\mathrm{T}} \nabla \boldsymbol{\Phi}_A(\sigma) A(t) \mathrm{d}V = \oiint_D \boldsymbol{\Phi}_A(\sigma) \frac{\partial \Phi(\sigma, t)}{\partial n} \mathrm{d}S \tag{7}$$

where $\nabla \boldsymbol{\Phi}_A(\sigma) = [\nabla \Phi_{A0}(\sigma), \nabla \Phi_{A1}(\sigma), \nabla \Phi_{A2}(\sigma), \ldots]$ is the gradient matrix of the shape function $\Phi_{Ar}(\sigma)$.

Using the boundary conditions (Equation (2)) and the orthogonality of the form function (Equation (4)):

$$\rho_0 \boldsymbol{M}_A \left[\ddot{\boldsymbol{A}}(t) + \boldsymbol{\Omega}_A^2 \boldsymbol{A}(t) \right] = \iint_D \boldsymbol{\Phi}_A(\sigma) u_n(\sigma, t) dS \tag{8}$$

where $\boldsymbol{M}_A = \mathrm{diag}[M_{A0}, M_{A1}, M_{A2}, \ldots]$ and $\boldsymbol{\Omega}_A = \mathrm{diag}[\omega_{A0}, \omega_{A1}, \omega_{A2}, \ldots]$ are the diagonal matrices of the modal mass M_{Ar} and the natural frequency ω_{Ar}, respectively.

For elastic cavity wall, it is usually a shell structure:

$$Sw_n(\sigma, t) + m_B \frac{\partial^2 w_n(\sigma, t)}{\partial t^2} = p_A(\sigma, t) - p_B(\sigma, t)(\sigma \in D_F) \tag{9}$$

where S is a linear differential operator characterizing the stiffness of the elastic cavity wall; m_B is the surface density of the elastic cavity wall; $w_n(\sigma, t)$ is the vibration displacement response of the elastic plate; $p_A(\sigma, t)$ and $p_B(\sigma, t)$ are the excitation (pressure) on the elastic cavity wall from the sound field inside the cavity and from the outside, respectively.

Similar to the case of Equation (1), if $p_A(\sigma, t) = 0$ and $p_B(\sigma, t) = 0$, Equation (9) has the modal solution $W_{Bj}(\sigma) \cdot \exp(j\omega_{Bj}t)$ $(j = 1, 2, \ldots)$, where ω_{Bj} is the jth order modal frequency of the elastic cavity wall and $W_{Bj}(\sigma)$ is the form function corresponding to ω_{Bj} with the following orthogonal properties:

$$\iint_{D_F} m_B W_{Bi}(\sigma) W_{Bj}(\sigma) dS = \begin{cases} 0 & (i \neq j) \\ M_{Bj} & (i = j) \end{cases} \tag{10}$$

where M_{Bj} $(j = 1, 2, 3, \ldots)$ is the modal mass of the thin-walled structure in vacuum.

The solution of Equation (9) is expressed in the form of a superposition of vibrations:

$$w_n(\sigma, t) = \sum_{j=1}^{\infty} W_{Bj}(\sigma)\beta_j(t) = [\boldsymbol{W}_B(\sigma)]^T \boldsymbol{\beta}(t) \quad (\sigma \in D_F) \tag{11}$$

where $\boldsymbol{W}_B(\sigma) = [W_{B1}(\sigma), W_{B2}(\sigma), W_{B3}(\sigma), \ldots]^T$ and $\boldsymbol{\beta}(t) = [\beta_1(t), \beta_2(t), \beta_3(t), \ldots]^T$ are the column vectors of $W_{Bj}(\sigma)$ and its corresponding modal coordinate $\beta_j(t)$, respectively.

Substituting the above equation into Equation (9) and using Equation (10):

$$\boldsymbol{M}_B \left[\ddot{\boldsymbol{\beta}}(t) + \boldsymbol{\Omega}_B^2 \boldsymbol{\beta}(t) \right] = \boldsymbol{Q}_A(t) + \boldsymbol{Q}_B(t) \tag{12}$$

where, $\boldsymbol{M}_B = \mathrm{diag}[M_{B0}, M_{B1}, M_{B2}, \ldots]$ and $\boldsymbol{\Omega}_B = \mathrm{diag}[\omega_{B0}, \omega_{B1}, \omega_{B2}, \ldots]$ are the diagonal matrices of the modal mass M_{Bj} and the natural frequency ω_{Bj}, respectively; $\boldsymbol{Q}_A(t)$ and $\boldsymbol{Q}_B(t)$ are the column vectors of the general forces loaded on the thin-walled structure in vacuum due to $p_A(\sigma, t)$ and $p_B(\sigma, t)$, respectively, and:

$$\boldsymbol{Q}_A(t) = \iint_{D_F} \boldsymbol{W}_B(\sigma) p_A(\sigma, t) dS \tag{13}$$

$$\boldsymbol{Q}_B(t) = -\iint_{D_F} \boldsymbol{W}_B(\sigma) p_B(\sigma, t) dS \tag{14}$$

Using Equation (5), $p_A(\sigma, t)$ is expressed as:

$$p_A(\sigma, t) = -\rho_0 \left. \frac{\partial \Phi}{\partial t} \right|_{\sigma \in D_F} = -\rho_0 [\boldsymbol{\Phi}_A(\sigma)]^T \Big|_{\sigma \in D_F} \dot{\boldsymbol{A}}(t) \tag{15}$$

Let the coupling matrix $\boldsymbol{L}$ be as follows:

$$\boldsymbol{L} = \iint_{D_F} \boldsymbol{\Phi}_A(\sigma) [\boldsymbol{W}_B(\sigma)]^T dS \tag{16}$$

Combining Equations (8), (12), (13), and (16) and $u_n(\sigma, t) = \partial w(\sigma, t)/\partial t$, the modal coordinate equation of the coupling system is obtained:

$$\begin{cases} \rho_0 M_A \left[\ddot{A}(t) + \Omega_A^2 A(t) \right] - L\dot{\beta}(t) = \mathbf{0} \\ M_B \left[\ddot{\beta}(t) + \Omega_B^2 \beta(t) \right] + \rho_0 L^T \dot{A}(t) = Q_B(t) \end{cases} \tag{17}$$

where $\mathbf{0}$ denotes a column vector with all 0 elements.

Let $\boldsymbol{\alpha}(t) = \dot{A}(t)$ and convert the above equation to the following form for an easy solution:

$$\begin{cases} \rho_0 M_A \left[\ddot{\boldsymbol{\alpha}}(t) + \Omega_A^2 \boldsymbol{\alpha}(t) \right] - L\ddot{\beta}(t) = \mathbf{0} \\ M_B \left[\ddot{\beta}(t) + \Omega_B^2 \beta(t) \right] + \rho_0 L^T \boldsymbol{\alpha}(t) = Q_B(t) \end{cases} \tag{18}$$

In the above equation, $Q_B(t) = 0$ for modal analysis and let:

$$\begin{cases} \boldsymbol{\alpha}(t) = \frac{1}{\rho_0} \left(\sqrt{M_A} \right)^{-1} \chi_A e^{j\omega t} \\ \beta(t) = \left(\Omega_B \sqrt{M_B} \right)^{-1} \chi_B e^{j\omega t} \end{cases} \tag{19}$$

where $\chi_A = [\chi_{A0}, \chi_{A1}, \chi_{A2}, \ldots]^T$ and $\chi_B = [\chi_{B0}, \chi_{B1}, \chi_{B2}, \ldots]^T$ are column vectors of the fluid-structure coupled modal shape coefficients χ_{Ar} $(r = 0, 1, 2, \ldots)$ and χ_{Bj} $(j = 0, 1, 2, \ldots)$ associated with the cavity sound field and the flexible boundary structure, respectively.

The eigenvalue problem can be obtained:

$$\Gamma\chi = \begin{bmatrix} \Gamma_{11} & \Gamma_{12} \\ \Gamma_{21} & \Gamma_{22} \end{bmatrix} \begin{bmatrix} \chi_A \\ \chi_B \end{bmatrix} = \omega^2 \begin{bmatrix} \chi_A \\ \chi_B \end{bmatrix} = \omega^2 \chi \tag{20}$$

where Γ represents a symmetric characteristic matrix which can be represented in blocks as $\Gamma_{11} = \Omega_A^2 + \left(\sqrt{M_A} \right)^{-1} L M_B^{-1} L^T \left(\sqrt{M_A} \right)^{-1}$, $\Gamma_{12} = \Gamma_{21}^T = \left(\sqrt{M_A} \right)^{-1} L \Omega_B \left(\sqrt{M_B} \right)^{-1}$, $\Gamma_{22} = \Omega_B^2$; χ is the vector of fluid-structure coupled modal shape coefficients.

The eigenvalues ω_{Ck}^2 $(k = 0, 1, 2, \ldots)$ of the matrix Γ, and its corresponding eigenvector $\left[\chi^{(k)} \right]^T = \left[\left\{ \chi_A^{(k)} \right\}^T, \left\{ \chi_B^{(k)} \right\}^T \right] = \left[\chi_{A0}^{(k)}, \chi_{A1}^{(k)}, \chi_{A2}^{(k)}, \ldots, \chi_{B0}^{(k)}, \chi_{B1}^{(k)}, \chi_{B2}^{(k)}, \ldots \right]$ are obtained from Equation (20), where ω_{Ck} is the kth order liquid-solid coupling mode frequency.

The velocity potential $\Phi_{Ck}(\sigma, t)$ of the acoustic field in the cavity and the vibration velocity $u_{Ck}(\sigma, t)$ of the cavity wall have a single-frequency vibration mode:

$$\begin{cases} \Phi_{Ck}(\sigma, t) = \frac{1}{j\omega_{Ck}\rho_0} [\Phi_A(\sigma)]^T \left(\sqrt{M_A} \right)^{-1} \chi_A e^{j\omega_{Ck}t} & (\sigma \in V) \\ u_{Ck}(\sigma, t) = j\omega_{Ck} [W_B(\sigma)]^T \left(\Omega_B \sqrt{M_B} \right)^{-1} \chi_B e^{j\omega_{Ck}t} & (\sigma \in D_F) \end{cases} \tag{21}$$

If there is a concentrated simple harmonic force $p_B(\sigma, t) = P_B e^{j\omega t} \delta(\sigma - \sigma_0)$ acting on the outside of the elastic wall plate of the chamber, the generalized force:

$$Q_B(t) = -\iint_{D_F} W_B(\sigma) P_B e^{j\omega t} \delta(\sigma - \sigma_0) dS = -P_B W_B(\sigma_0) e^{j\omega t} \tag{22}$$

The steady-state vibration response of the elastic wall plate:

$$u_n(\sigma, t) = j\omega [W_B(\sigma)]^T \left(\Omega_B \sqrt{M_B} \right)^{-1} X_B H T W_B(\sigma_0) P_B e^{j\omega t} \tag{23}$$

in the above equation, $T = X_A^H \left(\sqrt{M_A} \right)^{-1} L M_B^{-1} + X_B^H \Omega_B \left(\sqrt{M_B} \right)^{-1}$ is a transformation matrix; $X_A = \begin{bmatrix} \chi_A^{(0)} & \chi_A^{(1)} & \chi_A^{(2)} & \ldots \end{bmatrix}$ and $X_B = \begin{bmatrix} \chi_B^{(0)} & \chi_B^{(1)} & \chi_B^{(2)} & \ldots \end{bmatrix}$ are matrices consisting of $\chi_B^{(k)}$ and $\chi_B^{(k)}$, respectively, and the matrix compounded by X_A and X_B is denoted by $X = \begin{bmatrix} X_A^T & X_B^T \end{bmatrix}^T$; $H = \left(-\omega^2 M_C + \Omega_C^2 \cdot M_C \right)^{-1}$ is a transfer matrix, where, $M_C = X^H X = \text{diag}[M_{C0}, M_{C1} M_{C2}, \ldots]$ is the modal mass matrix of the coupling struc-

ture of the water-filled chamber and the elastic wall plate, and M_{Cr} $(r = 0, 1, 2, \ldots)$ is its rth order modal mass.

Admittance function on the elastic wall plate of the chamber:

$$Y(\sigma) = \frac{u_n(\sigma, t)}{P_B e^{j\omega t}} = j\omega [\boldsymbol{W}_B(\sigma)]^{\mathrm{T}} \left(\boldsymbol{\Omega}_B \sqrt{\boldsymbol{M}_B}\right)^{-1} \boldsymbol{X}_B \boldsymbol{HTW}_B(\sigma_0) \tag{24}$$

For rectangular water-filled chambers,

$$\omega_{Ar}^2 = \frac{K_0}{\rho_0} \left[\left(\frac{m_{Ar}\pi}{L_x}\right)^2 + \left(\frac{n_{Ar}\pi}{L_y}\right)^2 + \left(\frac{l_{Ar}\pi}{L_z}\right)^2 \right] \tag{25}$$

$$\Phi_{Ar}(\sigma) = \cos\left(\frac{m_{Ar}\pi x}{L_x}\right) \cos\left(\frac{n_{Ar}\pi y}{L_y}\right) \cos\left(\frac{l_{Ar}\pi z}{L_z}\right) \quad (\sigma(x, y, z) \in V) \tag{26}$$

To simplify the calculation, the boundary condition of simply supported on four sides is used here:

$$\omega_{Bj}^2 = \frac{\pi^4 E h^2}{12\rho(1 - \mu^2)} \left(\frac{m_{Bj}^2}{L_x^2} + \frac{n_{Bj}^2}{L_y^2}\right)^2 \tag{27}$$

$$W_{Bj}(\sigma) = \sin\left(m_{Bj}\pi x / L_x\right) \sin\left(n_{Bj}\pi y / L_y\right) \tag{28}$$

where L_x, L_y, L_z are the length, width, and height of the rectangular chamber, respectively; $\forall (m_{Ar}, n_{Ar}, l_{Ar}) \in N^3$ $(r = 0, 1, 2, \ldots)$ and ω_{Ar} satisfies $\omega_{A0} < \omega_{A1} < \omega_{A2} < \ldots$; E, ρ, h, and μ are the Young's modulus, mass density, thickness, and Poisson's ratio of the lower plate, respectively; $\forall (m_{Bj}, n_{Bj}) \in N_+^2$ $(j = 1, 2, 3, \ldots)$ and ω_{Bj} satisfies $\omega_{B1} < \omega_{B2} < \omega_{B3} < \ldots$.

2.2. Modeling of the Isolation Units

Let the isolation unit between the double-layer plate be a linear hybrid element of active and passive control with negative feedback, whose transfer characteristics are expressed by the four-terminal parameters:

$$\begin{bmatrix} \boldsymbol{F}_{Et} \\ \boldsymbol{U}_n' \end{bmatrix} = \begin{bmatrix} \boldsymbol{S}_{11} & \boldsymbol{S}_{12} \\ \boldsymbol{S}_{21} & \boldsymbol{S}_{22} \end{bmatrix} \begin{bmatrix} \boldsymbol{F}_{Eb} \\ \boldsymbol{U}_n \end{bmatrix} \tag{29}$$

where $\boldsymbol{F}_{Et}$ and $\boldsymbol{F}_{Eb}$ are the column vectors of the force of the active actuator acting on the upper and lower plates, respectively; $\boldsymbol{U}_n'$ and $\boldsymbol{U}_n$ are the column vectors of the velocity of the isolation device at the connection with the upper and lower plates, respectively; $\boldsymbol{S}_{ij}(i, j = 1, 2)$ is the four-terminal parameters matrix of the transfer characteristic, and:

$$\begin{cases} \boldsymbol{S}_{11} = \left(\boldsymbol{Z}_{11} + \boldsymbol{B}_{11}\boldsymbol{B}_{21}^{-1}\right)(\boldsymbol{I} + \boldsymbol{B}_{21}\boldsymbol{Z}_{21})^{-1}\boldsymbol{B}_{21} \\ \boldsymbol{S}_{12} = \boldsymbol{B}_{12} - \boldsymbol{B}_{11}\boldsymbol{B}_{21}^{-1}\boldsymbol{B}_{22} + \boldsymbol{Z}_{12} + \left(\boldsymbol{Z}_{11} + \boldsymbol{B}_{11}\boldsymbol{B}_{21}^{-1}\right)(\boldsymbol{I} + \boldsymbol{B}_{21}\boldsymbol{Z}_{21})^{-1}(\boldsymbol{B}_{22} - \boldsymbol{B}_{21}\boldsymbol{Z}_{22}) \\ \boldsymbol{S}_{21} = (\boldsymbol{I} + \boldsymbol{B}_{21}\boldsymbol{Z}_{21})^{-1}\boldsymbol{B}_{21} \\ \boldsymbol{S}_{22} = (\boldsymbol{I} + \boldsymbol{B}_{21}\boldsymbol{Z}_{21})^{-1}(\boldsymbol{B}_{22} - \boldsymbol{B}_{21}\boldsymbol{Z}_{22}) \end{cases} \tag{30}$$

In the above formula, $\boldsymbol{I}$ is the unit matrix; $\boldsymbol{B}_{ij}(i, j = 1, 2)$ is the four-terminal parameters matrix of the passive isolated element, and for the ideal elastic element, $\boldsymbol{B}_{11} = \boldsymbol{B}_{22} = \boldsymbol{I}$, $\boldsymbol{B}_{12} = 0$, $\boldsymbol{B}_{21} = j\omega \cdot \mathrm{diag}[1/K_1, 1/K_2, \ldots, 1/K_{N_I}]$, $K_l(l = 1, 2, \ldots, N_I)$ is the complex stiffness of the passive isolated element, $\boldsymbol{K} = \mathrm{diag}[K_1, K_2, \ldots, K_{N_I}]$ is the system stiffness matrix; $\boldsymbol{Z}_{ij}(i, j = 1, 2)$ is the equivalent impedance of the active isolating element, and the following equations hold:

$$\begin{cases} \boldsymbol{Z}_{11} = \boldsymbol{Z}_{21} = \frac{\boldsymbol{G}_4}{j\omega} + \boldsymbol{G}_5 + j\omega \boldsymbol{G}_6 \\ \boldsymbol{Z}_{12} = \boldsymbol{Z}_{22} + j\omega \boldsymbol{M}_a \\ \boldsymbol{Z}_{22} = \frac{\boldsymbol{G}_1 - \boldsymbol{G}_4}{j\omega} + (\boldsymbol{G}_2 - \boldsymbol{G}_5) + j\omega(\boldsymbol{G}_3 - \boldsymbol{G}_6) \end{cases} \tag{31}$$

where $M_a = \mathrm{diag}\big[m_{a1}, m_{a2}, m_{a3} \ldots, m_{aN_I}\big]$ is the diagonal matrix of the active actuator masses, and m_{al} is the mass of the lth actuator; G_1, G_2, and G_3 are the feedback parameter matrices of absolute displacement, velocity, and acceleration at the node where each isolation unit is coupled to the lower plate, respectively, and G_4, G_5, and G_6 are the feedback parameter matrices of relative displacement, velocity, and acceleration which the above node relatives to the node where each isolation unit is coupled to the upper plate, respectively, and:

$$
G_k = \begin{bmatrix}
\frac{k_{a1}e^{j\omega\tau_1'}}{R_1(1+j\omega\tau_1)}g_{11}^{(k)} & \frac{k_{a1}e^{j\omega\tau_1'}}{R_1(1+j\omega\tau_1)}g_{12}^{(k)} & \cdots & \frac{k_{a1}e^{j\omega\tau_1'}}{R_1(1+j\omega\tau_1)}g_{1N_I}^{(k)} \\
\frac{k_{a2}e^{j\omega\tau_2'}}{R_2(1+j\omega\tau_2)}g_{21}^{(k)} & \frac{k_{a2}e^{j\omega\tau_2'}}{R_2(1+j\omega\tau_2)}g_{22}^{(k)} & \cdots & \frac{k_{a2}e^{j\omega\tau_2'}}{R_2(1+j\omega\tau_2)}g_{2N_I}^{(k)} \\
\vdots & \vdots & \ddots & \vdots \\
\frac{k_{a2N_I}e^{j\omega\tau_{N_I}'}}{R_{N_I}(1+j\omega\tau_{N_I})}g_{N_I1}^{(k)} & \frac{k_{a2N_I}e^{j\omega\tau_{N_I}'}}{R_{N_I}(1+j\omega\tau_{N_I})}g_{N_I2}^{(k)} & \cdots & \frac{k_{a2N_I}e^{j\omega\tau_{N_I}'}}{R_{N_I}(1+j\omega\tau_{N_I})}g_{N_IN_I}^{(k)}
\end{bmatrix}
\tag{32}
$$

where $\tau_l = L_l / R_l$ is the electrical time constant of the lth active actuator; L_l and R_l are the inductance and resistance of its control circuit, respectively; τ_l' is the delay compensation generated by the controller for the lth active actuator; k_{al} is the power amplification gain parameter of the lth active actuator; and $g_{rs}^{(k)}$ $(r, s = 1, 2, \ldots, N_I; k = 1, 2, \ldots, 6)$ is the controller gain of the rth actuator relative to the feedback signal taken from the sth mounting node.

According to the principle of acoustic vibration isolation and the law of mass action, when $m_{al} \neq 0$, the vibration mass will increase, lowering the fundamental frequency of the system, expanding the effective sound insulation band to lower frequencies and increasing the sound insulation volume. However, the mass of the active actuator is much smaller than the mass of the acoustic cavity and the double-layer plate, such that the effect is almost negligible on the sound insulation of the system, so the M_a can be approximated to 0 in the actual simulation.

For each active actuator, the equivalent complex stiffness:

$$
\begin{aligned}
\Delta k^* &= j\omega \cdot \frac{k_{al}e^{j\omega\tau_l'}}{R_l(1+j\omega\tau_l)}g_{rs}^{(k)} = \frac{k_{al}\omega^2\tau g_{rs}^{(k)}}{R_l\sqrt{1+(\omega\tau_l)^2}}\Big(1+j\frac{1}{\omega\tau_l}\Big)e^{j\omega\tau_l'} \\
&= \Delta k_0(1+j\Delta\eta_0)e^{j\omega\tau_l'} = \Delta k_0\sqrt{1+(\Delta\eta_0)^2} \cdot e^{j(\arctan\Delta\eta_0+\omega\tau_l')}
\end{aligned}
\tag{33}
$$

where $\Delta\eta_0$ denotes the loss factor of the elastic support. Since the value of ω is extremely large, $\Delta\eta_0$ can be approximated as 0. Thus, the equivalent stiffness:

$$
\Delta k = \mathrm{Re}\{\Delta k^*\} = \Delta k_0\sqrt{1+(\Delta\eta_0)^2} \cdot \cos\big(\arctan\Delta\eta_0 + \omega\tau_l'\big)
\tag{34}
$$

Since the time lag $\omega\tau_l'$ of the active actuator is extremely small, it tends to 0, it can be neglected in the actual simulation calculation. The time lag does not improve the control effect. When $\omega^{\tau_l'}$ is large enough, the control of the active actuator on the amount of stiffness change does not achieve the expected effect, reducing the sound insulation performance of the system. In extreme cases of inappropriate control, it can even cause system instability. Therefore, the time lag cannot be artificially added to the active actuator, except for the almost negligible self-contained time lag.

2.3. Calculation of the Transferred Power Flow of the Coupling System

Let the external excitation $p_E(\sigma, t) = P_E \cdot e^{j\omega t}$ acting on the upper plate be a homogeneous simple harmonic force (pressure).

For the upper plate, its vibration differential equation:

$$\nabla^4 w'_n(\sigma, t) + \rho h \frac{\partial^2 w'_n(\sigma, t)}{\partial t^2} = \sum_{l=1}^{N_I} F_{El}(t)\delta(\sigma - \sigma_l) - P_E e^{j\omega t} \tag{35}$$

where $w'_n(\sigma, t)$ is the vibration displacement response of the upper plate; $F_{El}(t)$ is the force of the lth isolation unit on the upper plate.

The oscillation superposition method is used to make $w'_n(\sigma, t)$ expressed as a series solution $w'_n(\sigma, t) = \sum_{j=1}^{\infty} W_{Ej}(\sigma)q_{Ej}(t)$, and its normal vibration velocity $u'_n(\sigma, t) = \dot{w}'_n(\sigma, t)$, so it is obtained:

$$\boldsymbol{U}'_n = \left[u'_n(\sigma_1), u'_n(\sigma_2), \ldots, u'_n(\sigma_{N_I})\right]^T = -j\omega\left(\overline{\boldsymbol{W}}_E^T \boldsymbol{H}_E \boldsymbol{Q}_E + \overline{\boldsymbol{W}}_E^T \boldsymbol{H}_E \overline{\boldsymbol{W}}_E \boldsymbol{F}_{Et}\right) = \boldsymbol{A}^{(1)}\boldsymbol{Q}_E + \boldsymbol{A}^{(2)}\boldsymbol{F}_{Et} \tag{36}$$

In the equation, $\boldsymbol{H}_E = \left(-\omega^2 \boldsymbol{M}_E + \boldsymbol{\Omega}_E \boldsymbol{M}_E\right)^{-1}$ is a transfer matrix; $\boldsymbol{M}_E = \mathrm{diag}[M_{E1}, M_{E2}, M_{E3}, \ldots]$ and $\boldsymbol{\Omega}_E = \mathrm{diag}[\omega_{E1}, \omega_{E2}, \omega_{E3}, \ldots]$ are the diagonal matrices of the modal mass M_{Ej} and the natural frequency ω_{Ej} of the upper plate, respectively; $\overline{\boldsymbol{W}}_E = [\boldsymbol{W}_E(\sigma_1), \boldsymbol{W}_E(\sigma_2), \ldots, \boldsymbol{W}_E(\sigma_l)]$ is a matrix consisting of $\boldsymbol{W}_E(\sigma)$, and $\boldsymbol{W}_E(\sigma) = [W_{E1}(\sigma), W_{E2}(\sigma), W_{E3}(\sigma), \ldots]^T$ is the column vector of the form function $W_{Ej}(\sigma)$ $(j = 1, 2, 3, \ldots)$ of the upper plate; $\boldsymbol{Q}_E$ is the column vector of generalized forces acting on the upper plate.

For the lower plate and chamber coupling unit,

$$\boldsymbol{U}_n = \boldsymbol{C} \cdot \boldsymbol{F}_{Eb} = [C_{rs}]\boldsymbol{F}_{Eb} \tag{37}$$

where $C_{rs} = j\omega[\boldsymbol{W}_B(\sigma_r)]^T (\boldsymbol{\Omega}_B \sqrt{\boldsymbol{M}_B})^{-1} \boldsymbol{X}_B \boldsymbol{HT} \boldsymbol{W}_B(\sigma_s)$, $(r, s = 1, 2, \ldots, N_I)$.

The admittance matrix $\boldsymbol{C}$ can in turn be expressed as:

$$\boldsymbol{C} = j\omega\overline{\boldsymbol{W}}_B^T \left(\boldsymbol{\Omega}_B \sqrt{\boldsymbol{M}_B}\right)^{-1} \boldsymbol{X}_B \boldsymbol{HT} \overline{\boldsymbol{W}}_B \tag{38}$$

where $\overline{\boldsymbol{W}}_B = [\boldsymbol{W}_B(\sigma_1), \boldsymbol{W}_B(\sigma_2), \ldots, \boldsymbol{W}_B(\sigma_l)]$ is a matrix consisting of $\boldsymbol{W}_B(\sigma)$.

From Equations (29), (36) and (37), the following equations can be obtained:

$$\boldsymbol{F}_{Eb} = \left[\boldsymbol{S}_{21} + \boldsymbol{S}_{22}\boldsymbol{C} - \boldsymbol{A}^{(2)}(\boldsymbol{S}_{11} + \boldsymbol{S}_{12}\boldsymbol{C})\right]^{-1} \boldsymbol{A}^{(1)}\boldsymbol{Q}_E \tag{39}$$

$$\boldsymbol{U}_n = \boldsymbol{C}\left[\boldsymbol{S}_{21} + \boldsymbol{S}_{22}\boldsymbol{C} - \boldsymbol{A}^{(2)}(\boldsymbol{S}_{11} + \boldsymbol{S}_{12}\boldsymbol{C})\right]^{-1} \boldsymbol{A}^{(1)}\boldsymbol{Q}_E \tag{40}$$

$$\boldsymbol{F}_{Et} = (\boldsymbol{S}_{11} + \boldsymbol{S}_{12}\boldsymbol{C})\left[\boldsymbol{S}_{21} + \boldsymbol{S}_{22}\boldsymbol{C} - \boldsymbol{A}^{(2)}(\boldsymbol{S}_{11} + \boldsymbol{S}_{12}\boldsymbol{C})\right]^{-1} \boldsymbol{A}^{(1)}\boldsymbol{Q}_E \tag{41}$$

$$\boldsymbol{U}'_n = (\boldsymbol{S}_{21} + \boldsymbol{S}_{22}\boldsymbol{C})\left[\boldsymbol{S}_{21} + \boldsymbol{S}_{22}\boldsymbol{C} - \boldsymbol{A}^{(2)}(\boldsymbol{S}_{11} + \boldsymbol{S}_{12}\boldsymbol{C})\right]^{-1} \boldsymbol{A}^{(1)}\boldsymbol{Q}_E \tag{42}$$

The total input power flow for external excitation:

$$\begin{aligned} P_{in} &= \iint_{D_E} \frac{1}{2}\mathrm{Re}\{u'_n(\sigma)P_E^*(\sigma)\}\mathrm{d}S \\ &= -\frac{\omega}{2}\mathrm{Re}\{j\iint_{D_E} P_E^*(\sigma)[\boldsymbol{W}_E^T(\sigma)\boldsymbol{H}_E\boldsymbol{Q}_E + \boldsymbol{W}_E^T(\sigma)\boldsymbol{H}_E\overline{\boldsymbol{W}}_E\boldsymbol{F}_{Et}]\mathrm{d}S\} \\ &= \frac{\omega}{2}\mathrm{Re}\{j\boldsymbol{Q}_E^H\boldsymbol{H}_E(\boldsymbol{Q}_E + \overline{\boldsymbol{W}}_E\boldsymbol{F}_{Et})\} \end{aligned} \tag{43}$$

where the superscript " $*$ " indicates that the conjugate is taken.

Power flow into the lower plate-water-filled acoustic cavity coupling system:

$$P_{\mathrm{c}} = \frac{1}{2}\mathrm{Re}\left\{ \boldsymbol{F}_{\mathrm{Eb}}^{\mathrm{H}} \boldsymbol{U}_n \right\} \tag{44}$$

Power flow into the water-filled acoustic cavity:

$$
\begin{aligned}
P_{\mathrm{tr}} &= \iint\limits_{D_{\mathrm{F}}} \frac{1}{2}\mathrm{Re}\left\{ U_n(\sigma) P^*(\sigma) \big|_{\sigma \in D_{\mathrm{F}}} \right\} \mathrm{d}S \\
&= \frac{\rho_0 c_0 \omega}{2}\mathrm{Re}\left\{ \mathrm{j}\boldsymbol{P}_{\mathrm{B}}^{\mathrm{H}} \boldsymbol{T}^{\mathrm{H}} \boldsymbol{H}^* \boldsymbol{X}_{\mathrm{A}}^{\mathrm{H}} \left(\sqrt{\boldsymbol{M}_{\mathrm{A}}} \right)^{-1} \boldsymbol{L}\left(\boldsymbol{\Omega}_{\mathrm{B}}\sqrt{\boldsymbol{M}_{\mathrm{B}}} \right)^{-1} \boldsymbol{X}_{\mathrm{B}} \boldsymbol{H} \boldsymbol{T} \boldsymbol{P}_{\mathrm{B}} \right\}
\end{aligned}
\tag{45}
$$

where $\boldsymbol{P}_{\mathrm{B}} = -\iint_{D_{\mathrm{F}}} \boldsymbol{W}_{\mathrm{B}}(\sigma)\left[\sum\limits_{l=1}^{N_{\mathrm{I}}} F_{\mathrm{E}l}\delta(\sigma - \sigma_l) \right] \mathrm{d}S = -\overline{\boldsymbol{W}}_{\mathrm{B}} \boldsymbol{F}_{\mathrm{Eb}}$.

Therefore, Equation (45) is further expressed as:

$$P_{\mathrm{tr}} = \frac{\rho_0 c_0 \omega}{2}\mathrm{Re}\left\{ \mathrm{j}\boldsymbol{F}_{\mathrm{Eb}}\overline{\boldsymbol{W}}_{\mathrm{B}}^{\mathrm{T}} \boldsymbol{T}^{\mathrm{H}} \boldsymbol{H}^* \boldsymbol{X}_{\mathrm{A}}^{\mathrm{H}}\left(\sqrt{\boldsymbol{M}_{\mathrm{A}}} \right)^{-1} \boldsymbol{L}\left(\boldsymbol{\Omega}_{\mathrm{B}}\sqrt{\boldsymbol{M}_{\mathrm{B}}} \right)^{-1} \boldsymbol{X}_{\mathrm{B}} \boldsymbol{H} \boldsymbol{T} \overline{\boldsymbol{W}}_{\mathrm{B}} \boldsymbol{F}_{\mathrm{Eb}} \right\} \tag{46}$$

The ratio of P_{tr} to P_{in} reflects the absorption coefficient of the cavity and provides an evaluation of the energy absorption level of the sound insulation system. In acoustics, the average power flow per unit area is called sound intensity, and the sound intensity is proportional to the amplitude of the sound pressure. The sound pressure measured on a logarithmic scale is defined as the sound pressure level [28]. Therefore, there is a certain proportional relationship between the average power flow and the average sound pressure level [29]. Therefore, the average power flow, the average sound pressure level and the absorption coefficient can all evaluate the sound insulation performance of the system. However, due to the limited time and space, only different active control strategies are discussed for the system in this paper. So only the average power flow into the water-filled acoustic cavity is calculated and analyzed in the numerical simulation below.

3. Simulation Calculation and Analysis of Active Feedback Sound Insulation Strategy in Frequency Domain

In this paper, the average energy input P_{tr} in the acoustic cavity is calculated by a MATLAB environment simulation and used as an evaluation index of the sound insulation effect. In order not to lose the generality of the system, the active sound insulation units are laid out symmetrically, and the number of arrangements is four. As mentioned in Section 2.2, the time lag $\omega \tau_l \prime$ of the active actuator can be neglected in the simulation due to its extremely small value. To simplify the simulation and analysis, all active actuators are used with the same specifications, so that the electrical time constant $\tau_1 = \tau_2 = \tau_3 = \tau_4 = \tau$, the amplifier gain parameter $k_{\mathrm{a}1} = k_{\mathrm{a}2} = k_{\mathrm{a}3} = k_{\mathrm{a}4} = k_{\mathrm{a}}$, and the control circuit resistance $R_1 = R_2 = R_3 = R_4 = R$. Additionally, $g_{rs}^{(k)} = 0$ ($r, s = 1, 2, 3, 4$; $k = 1, 2, \ldots, 6$), except for $g_{11}^{(k)}$, $g_{22}^{(k)}$, $g_{33}^{(k)}$, and $g_{44}^{(k)}$. Let $K = k_{\mathrm{a}}/(1 + \mathrm{j}\omega\tau)$. Then, Equation (32) can be simplified as follows:

$$\boldsymbol{G}_k = \frac{K}{R}\begin{bmatrix} g_{11}^{(k)} & & & \\ & g_{22}^{(k)} & & \\ & & g_{33}^{(k)} & \\ & & & g_{44}^{(k)} \end{bmatrix} \tag{47}$$

From Equation (47), the feedback parameter matrixes $\boldsymbol{G}_1$, $\boldsymbol{G}_2$, $\boldsymbol{G}_3$, $\boldsymbol{G}_4$, $\boldsymbol{G}_5$ and $\boldsymbol{G}_6$ are only linearly related to $g_{11}^{(k)}$, $g_{22}^{(k)}$, $g_{33}^{(k)}$, and $g_{44}^{(k)}$. To further facilitate variable analysis, let all the actuators of the system have the same feedback signal controller gain at their respective installation points, that is $g_{11}^{(k)} = g_{22}^{(k)} = g_{33}^{(k)} = g_{44}^{(k)}$.

The settings of the system's basic parameters are given here, as shown in Table 1.

Table 1. Setting of system's basic parameters.

Vibration Isolation System	Basic Parameters	Symbols	Units	Numerical Values	Remarks
Rectangular chamber	Length	L_x	m	0.4	
	Width	L_y	m	0.6	
	Height	L_z	m	0.7	
	Density of the medium	ρ_0	kg/m^3	1000	
	Sound velocity	c_0	m/s	1500	
Double-layer structure	Thickness of each layer	h	cm	0.5	Stainless steel plate
	Young's modulus of elasticity	E	N/m^2	2.0×10^{11}	
	Density	ρ	kg/m^3	7.8×10^3	
	Poisson's ratio	μ		0.28	
	Damping ratio	ζ		0.01	

To completely represent the effect of the continuous variation of the feedback parameter values in the frequency domain on the average energy transfer P_{tr} in the acoustic cavity, the P_{tr} values in the frequency domain range from 0 to 1000 Hz for different values of the feedback parameters are calculated numerically to generate the comparison graphs in this section. The 3D image of surf (X, Y, Z) and its corresponding plane three views are generated by simulation, where the feedback parameter value $g_{11}^{(k)}$ —frequency *Fre* —average energy input P_{tr} in the acoustic cavity is the X-Y-Z axis of the 3D image. The 2D images and 3D images are analyzed by comprehensive comparison, as shown in Figures 2–7.
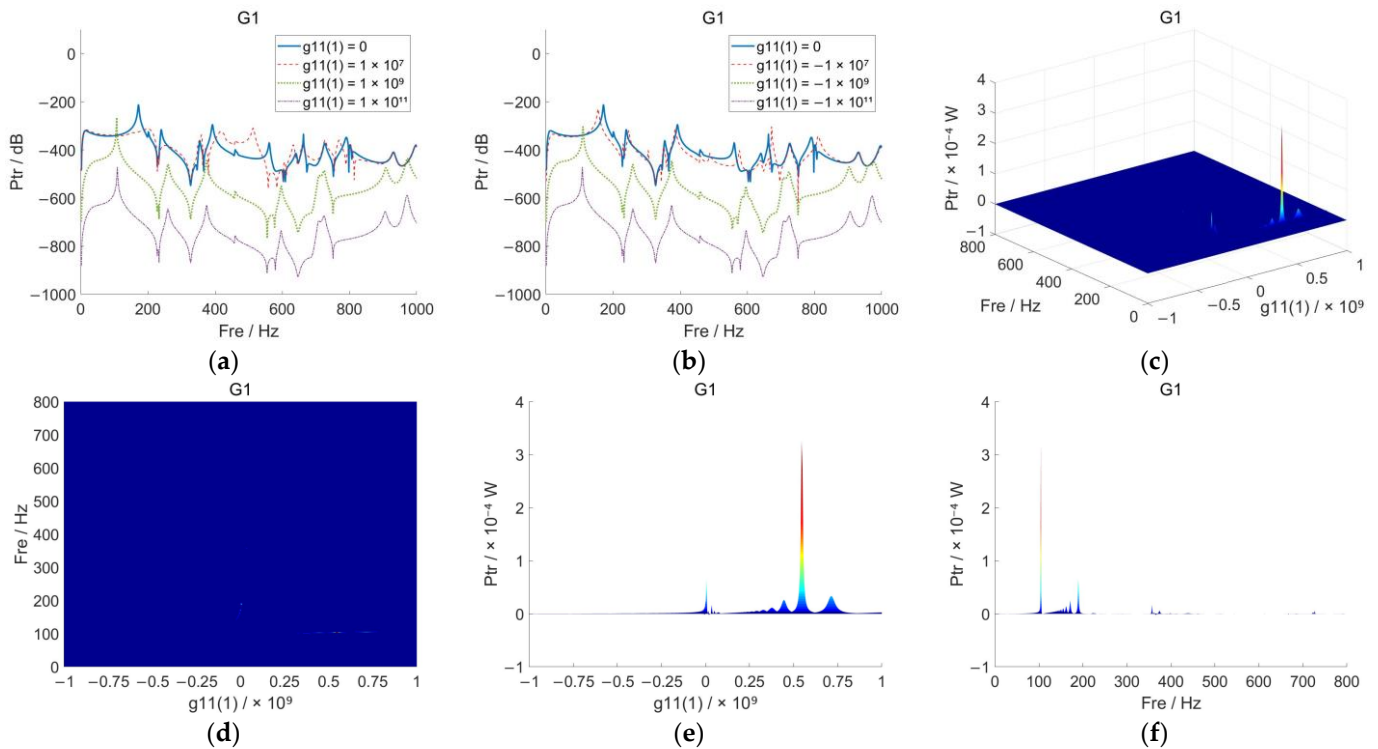
Figure 2. The 2D view and 3D view of $g_{11}^{(1)}$ — *Fre* — P_{tr} under the absolute displacement feedback control method ($g_{11}^{(1)} \in \left(-10^{11}, \ 10^{11}\right)$, the step size is set to 1×10^7): (**a**) comparison of P_{tr} curves under $g_{11}^{(1)} > 0$; (**b**) comparison of P_{tr} curves under $g_{11}^{(1)} < 0$; (**c**) the 3D view of P_{tr} curve under continuous variation of $g_{11}^{(1)}$; (**d**) X-Y plane view; (**e**) X-Z plane view; (**f**) Y-Z plane view.
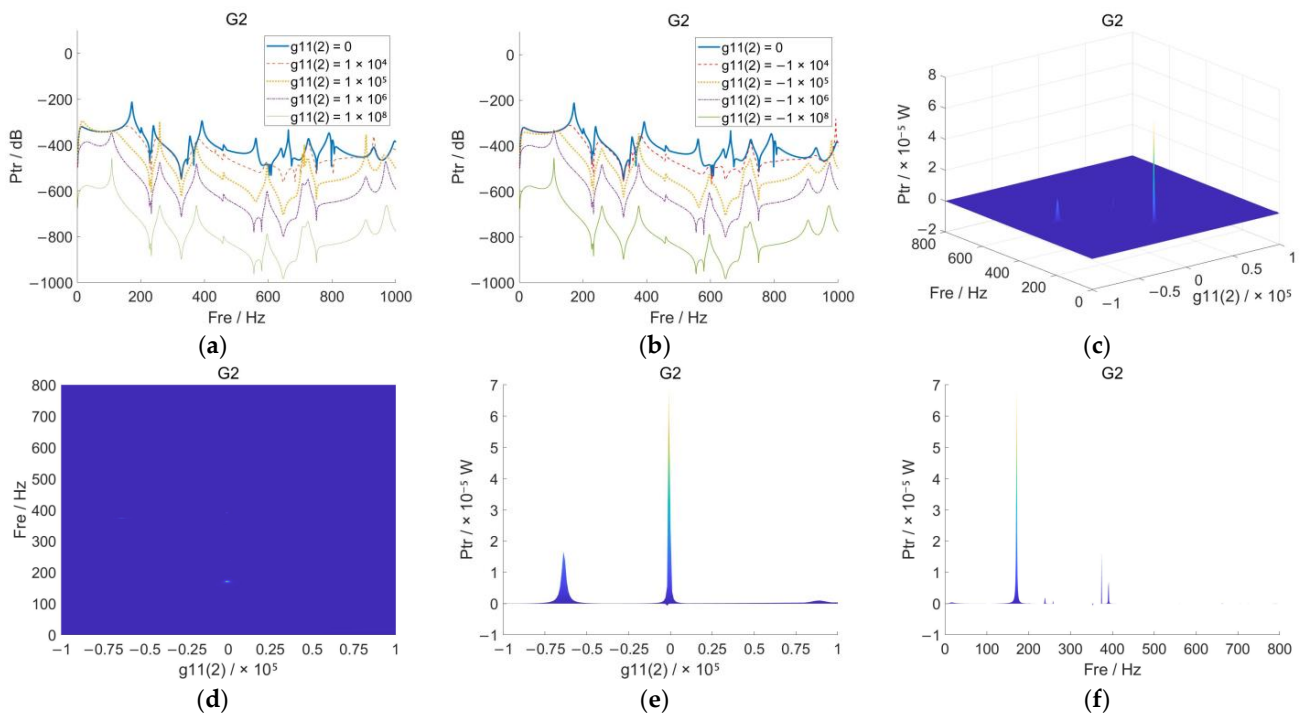
Figure 3. The 2D view and 3D view of $g_{11}^{(2)} - Fre - P_{\text{tr}}$ under the absolute velocity feedback control method ($g_{11}^{(2)} \in (-10^5, 10^5)$, the step size is set to 1×10^2): (**a**) comparison of P_{tr} curves under $g_{11}^{(2)} > 0$; (**b**) comparison of P_{tr} curves under $g_{11}^{(2)} < 0$; (**c**) the 3D view of P_{tr} curve under continuous variation of $g_{11}^{(2)}$; (**d**) X-Y plane view; (**e**) X-Z plane view; (**f**) Y-Z plane view.
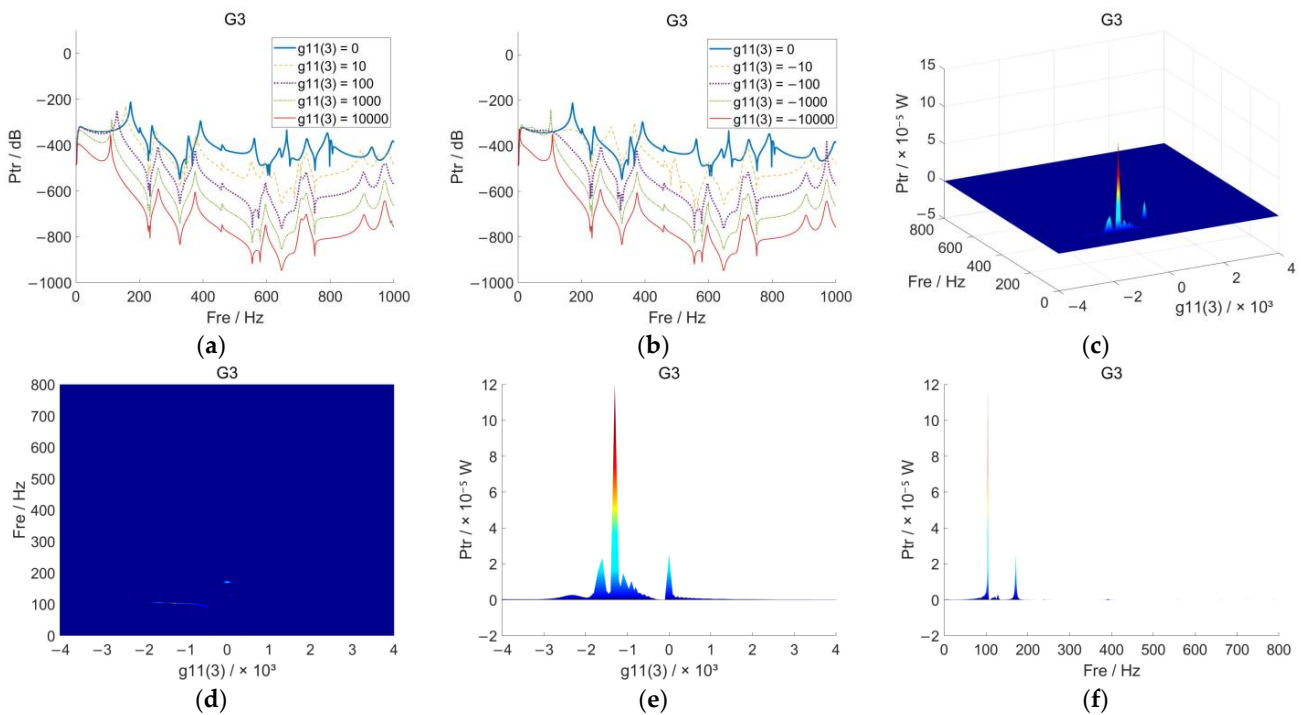
Figure 4. The 2D view and 3D view of $g_{11}^{(3)} - Fre - P_{\text{tr}}$ under the absolute acceleration feedback control method ($g_{11}^{(3)} \in (-10^4, 10^4)$, the step size is set to 10): (**a**) comparison of P_{tr} curves under $g_{11}^{(3)} > 0$; (**b**) comparison of P_{tr} curves under $g_{11}^{(3)} < 0$; (**c**) the 3D view of P_{tr} curve under continuous variation of $g_{11}^{(3)}$; (**d**) X-Y plane view; (**e**) X-Z plane view; (**f**) Y-Z plane view.
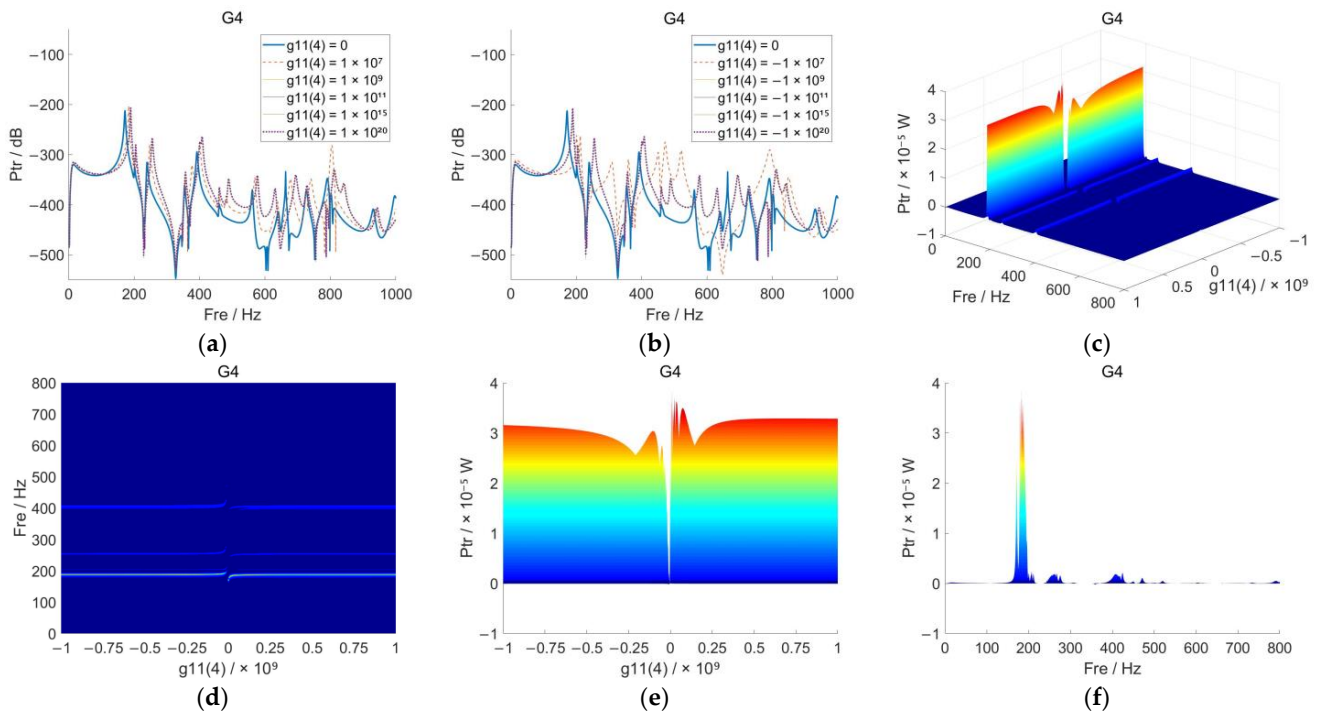
Figure 5. The 2D view and 3D view of $g_{11}^{(4)}$ — Fre — P_{tr} under the relative displacement feedback control method ($g_{11}^{(4)} \in (-10^9, \; 10^9)$, the step size is set to 1×10^6): (**a**) comparison of P_{tr} curves under $g_{11}^{(4)} > 0$; (**b**) comparison of P_{tr} curves under $g_{11}^{(4)} < 0$; (**c**) the 3D view of P_{tr} curve under continuous variation of $g_{11}^{(4)}$; (**d**) X-Y plane view; (**e**) X-Z plane view; (**f**) Y-Z plane view.
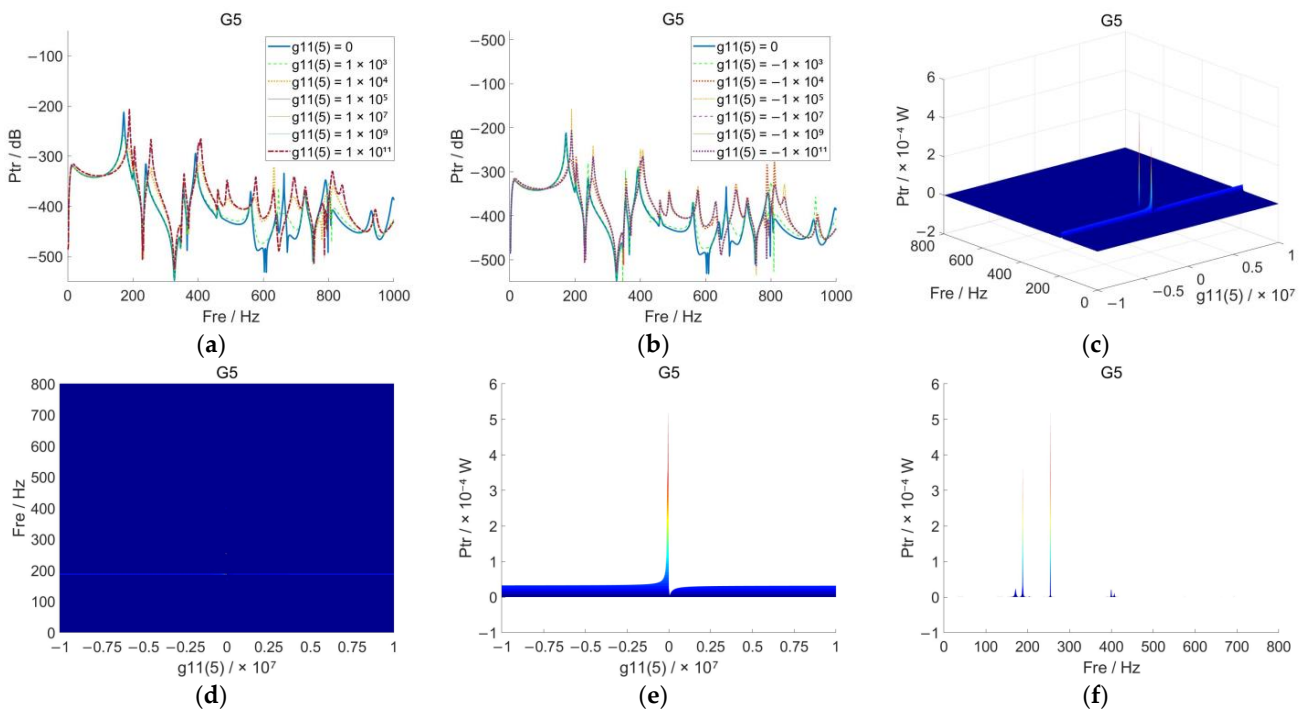
Figure 6. The 2D view and 3D view of $g_{11}^{(5)}$ — Fre — P_{tr} under the relative velocity feedback control method ($g_{11}^{(5)} \in (-10^7, \; 10^7)$, the step size is set to 1×10^4): (**a**) comparison of P_{tr} curves under $g_{11}^{(5)} > 0$; (**b**) comparison of P_{tr} curves under $g_{11}^{(5)} < 0$; (**c**) the 3D view of P_{tr} curve under continuous variation of $g_{11}^{(5)}$; (**d**) X-Y plane view; (**e**) X-Z plane view; (**f**) Y-Z plane view.
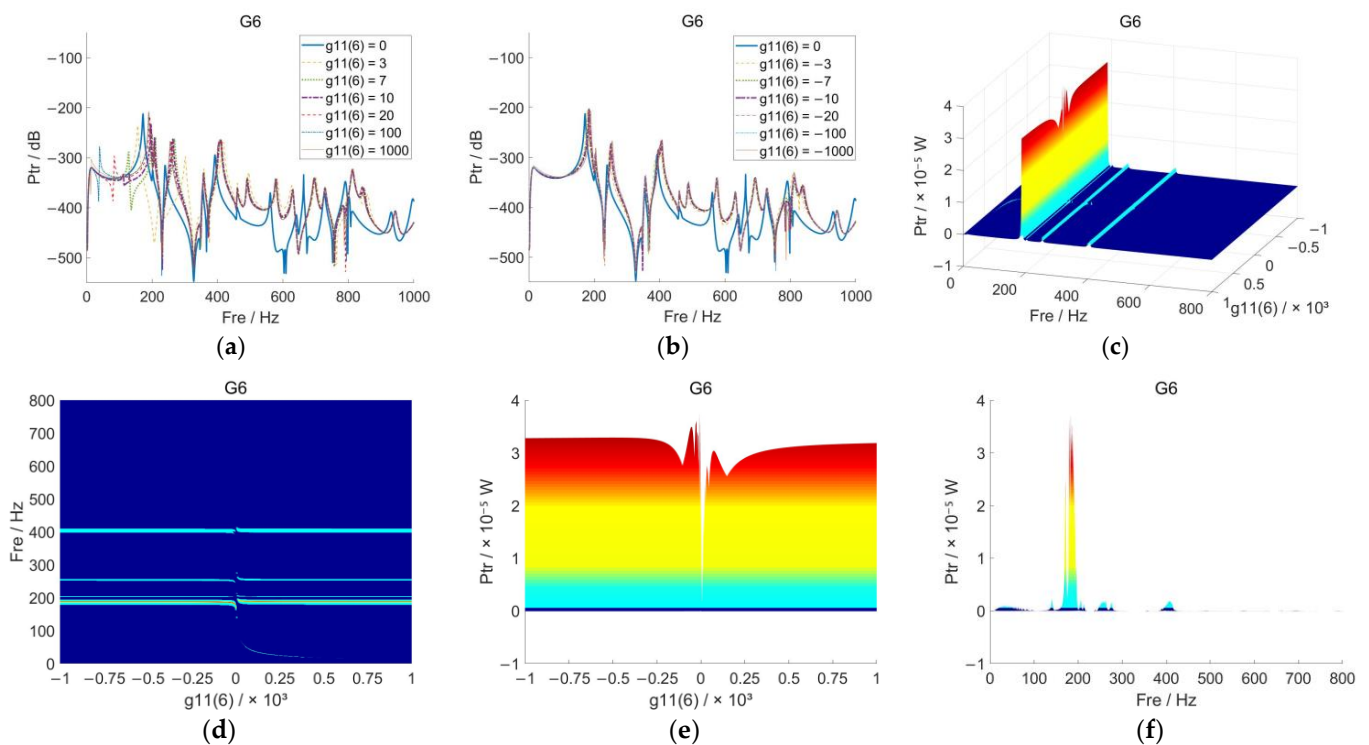
Figure 7. The 2D view and 3D view of $g_{11}^{(6)}$ — *Fre* — P_{tr} under the relative acceleration feedback control method ($g_{11}^{(6)} \in (-10^3, 10^3)$, the step size is set to 1): (**a**) comparison of P_{tr} curves under $g_{11}^{(6)} > 0$; (**b**) comparison of P_{tr} curves under $g_{11}^{(6)} < 0$; (**c**) the 3D view of P_{tr} curve under continuous variation of $g_{11}^{(6)}$; (**d**) X-Y plane view; (**e**) X-Z plane view; (**f**) Y-Z plane view.

In Figures 2–7, both Figures (a) and (b) show the trends and comparisons of the curves of P_{tr} in the frequency domain from 0 to 1000 Hz for several different sets of feedback parameter values at $g_{11}^{(k)} > 0$ and $g_{11}^{(k)} < 0$, respectively. To more clearly and intuitively represent the distribution and variation of resonance peaks with smaller values, the scale value of the vertical coordinate is $20 \cdot \lg(P_{tr}/P_{ref})$, where P_{ref} is a reference power flow and takes the value of 1. The unit is also converted to dimensionless dB. Both Figures (c) show the distribution of the main resonance peak in the frequency domain for continuously varying $g_{11}^{(k)}$. Figures (d), (e), and (f) show the planar views of Figures (c) in the X-Y, X-Z, and Y-Z directions, respectively. Here, there is no logarithmic treatment of the vertical coordinate P_{tr}, and the order of magnitude of the P_{tr} values at the main resonance peaks in the low-frequency region is much larger than at other places. Therefore, except for these main resonance peaks, the P_{tr} values at other places are basically shown to converge to zero in these figures.

In this simulation example, the area near the first order resonance peak is defined as the low-frequency region, which ranges from about 0 to 200 Hz; the area where the second- and third-order resonance peaks are located is defined as the medium-frequency region, which ranges from about 200 to 400 Hz; the area after the third-order resonance peak is defined as the high-frequency region, which ranges from about 400 Hz to more. The specific analysis of Figures 2–7 is as follows.

As shown in Figure 2a,b, the overall P_{tr} curve shows a gradual sinking trend as $\left| g_{11}^{(1)} \right|$ increases, but there is a local rising in the high-frequency region at $g_{11}^{(1)} = 1.0 \times 10^7$. In the low- and medium-frequency region, the first resonance peak gradually shifts to the left with the increase of $\left| g_{11}^{(1)} \right|$, and its peak is also reduced. In the high-frequency region, $g_{11}^{(1)}$ does not make the problem solved, where the system's higher-order modes are excited and trigger a large number of peaks. This indicates that properly assigned $g_{11}^{(1)}$ can optimize

the system's sound insulation in the low- and medium-frequency region, but improperly assigned $g_{11}^{(1)}$ may deteriorate it instead. However, the effect of $g_{11}^{(1)}$ on the optimization of system sound insulation in the high-frequency region is not obvious. In this simulation, the significant effective sound insulation frequency range is about 1~400 Hz with proper assignment of $g_{11}^{(1)}$.

Combining Figure 2c–f, when $g_{11}^{(1)} < 0$ or $1 \times 10^7 < g_{11}^{(1)} < 0.2 \times 10^9$ or $g_{11}^{(1)} > 0.8 \times 10^9$, the first resonance peak is basically eliminated, which indicates that the sound insulation effect of the system is well. When $0.2 \times 10^9 < g_{11}^{(1)} < 0.8 \times 10^9$, the first resonance peaks still exist, but they all move to the lower-frequency region, which indicates that the system has a certain sound insulation effect. However, from the peak perspective, the first resonance peak is significantly raised at $0.5 \times 10^9 < g_{11}^{(1)} < 0.6 \times 10^9$. This indicates that the $g_{11}^{(1)}$ at this point exacerbates the resonance effect and deteriorates the system's sound insulation.

In summary, the absolute displacement feedback control method plays a significant role for the system's sound insulation in the low- and medium-frequency domain. The vast majority of the feedback parameter values are within the effective range of values and can optimize the system's sound insulation in the low- and medium-frequency region. However, this control method is not ideal for system's sound insulation in the high-frequency region, and even some inappropriate values of feedback parameters can deteriorate the system's high-frequency sound insulation instead.

As shown in Figure 3a,b, the overall P_{tr} curve shows a gradual sinking trend as $\left| g_{11}^{(2)} \right|$ increases. In the low- and medium-frequency regions, the first resonance peak gradually shifts to the left with the increase of $\left| g_{11}^{(2)} \right|$, and its peak is also reduced. In the high-frequency region, $g_{11}^{(2)}$ does not make the problem solved, where the system's higher-order modes are excited and trigger a large number of peaks. This indicates that properly assigned $g_{11}^{(2)}$ can optimize the system's sound insulation in the low- and medium-frequency region. However, the effect of $g_{11}^{(2)}$ on the optimization of system sound insulation in the high-frequency region is not obvious. In this simulation, the significant effective sound insulation frequency range is about 1~400 Hz with proper assignment of $g_{11}^{(2)}$.

Combining Figure 3c–f, when $g_{11}^{(2)} - 0.1 \times 10^5$ or $g_{11}^{(2)} > 0.1 \times 10^5$, the first resonance peak is basically eliminated, which indicates that the sound insulation effect of the system is well. When $-0.8 \times 10^5 < g_{11}^{(2)} < 0.1 \times 10^5$ (except 0), the first resonance peaks still exist, but they all move to the lower-frequency region, which indicates that the system has a certain sound insulation effect.

In summary, the absolute velocity feedback control method plays a significant role for the system's sound insulation in the low- and medium-frequency domain. Almost all feedback parameter values are validly taken and can optimize the system's sound insulation in the low and medium frequency region. However, this control method is not ideal for system's sound insulation in the high-frequency region.

As shown in Figure 4a,b, the overall P_{tr} curve shows a gradual sinking trend as $\left| g_{11}^{(3)} \right|$ increases. In the low- and medium-frequency regions, the first resonance peak gradually shifts to the left with the increase of $\left| g_{11}^{(3)} \right|$, and its peak is also reduced. In the high-frequency region, the number of large peaks triggered by the excitation of the higher-order modes of the system is reduced. This indicates that a properly assigned $g_{11}^{(3)}$ has a significant optimization effect on the system's sound insulation in both the low and medium-frequency regions as well as the high-frequency region. In this simulation, the significant effective sound insulation frequency range is 1~1000 Hz with proper assignment of $g_{11}^{(3)}$.

Combining Figure 4c–f, when $g_{11}^{(3)} < -3000$ or $g_{11}^{(3)} > 1000$, the first resonance peak is basically eliminated, which indicates that the sound insulation effect of the system is well. When $-3000 < g_{11}^{(3)} < 1000$ (except 0), the first resonance peaks still exist, but they

all move to the lower-frequency region, which indicates that the system has a certain sound insulation effect. However, from the peak perspective, the first resonance peak is significantly raised at $-2700 < g_{11}^{(3)} < -2600$. This indicates that the $g_{11}^{(3)}$ at this point exacerbates the resonance effect and deteriorates the system's sound insulation.

In summary, the absolute acceleration feedback control method plays a significant role for the system's sound insulation in the low- and medium-frequency domain. The vast majority of the feedback parameter values are within the effective range of values and can optimize the system's sound insulation in the low- and medium-frequency region. At the same time, this control method produces a significant effect on the system's high-frequency sound insulation. In addition, the average energy input amplitude-frequency response of the system is most sensitive under the absolute acceleration feedback control method compared to the absolute displacement and velocity feedback control methods.

As shown in Figure 5a,b, the overall P_{tr} curve has a slight rightward shift as $\left| g_{11}^{(4)} \right|$ increases. In the high-frequency region, $g_{11}^{(4)}$ does not make the problem solved, where the system's higher-order modes are excited and trigger a large number of peaks, and even the P_{tr} value increases slightly. From the point of view of resonant frequencies, improperly assigned $g_{11}^{(4)}$ can slightly deteriorate the system's sound insulation in the low- and medium-frequency regions. From the point of view of the average energy input value, improperly assigned $g_{11}^{(4)}$ can also deteriorate the system's sound insulation in the high-frequency region. In this simulation, the significant effective sound insulation frequency range is about 1~400 Hz with proper assignment of $g_{11}^{(4)}$.

Combining Figure 5c,f, in the narrow region on the right side very close to $g_{11}^{(4)} = 0$, the first resonance peak is basically eliminated, which indicates that the sound insulation effect of the system is well. Outside this narrow region, although the peak is reduced compared to that at $g_{11}^{(4)} = 0$, it is not very significant. In addition to the first resonance peak, the second and third resonance peaks are still present. Therefore, the sound insulation effect of the system is not ideal at this time.

In summary, the effective range of the feedback parameters for the relative displacement feedback control method is narrow. Within the effective range of values, it can improve the system's low- and medium-frequency sound insulation capability. However, outside the effective range, it does not play a role in the system's low- and medium-frequency sound insulation, and even plays a deteriorating role for the system's high-frequency sound insulation. On the whole, the sound insulation effect under the relative displacement feedback control method is worse than that of the absolute displacement feedback control method.

As shown in Figure 6a,b, the overall P_{tr} curve has a slight rightward shift as $\left| g_{11}^{(5)} \right|$ increases. In the high-frequency region, $g_{11}^{(5)}$ does not make the problem solved, where the system's higher-order modes are excited and trigger a large number of peaks, and even the P_{tr} value increases slightly. From the point of view of resonant frequencies, improperly assigned $g_{11}^{(5)}$ can slightly deteriorate the system's sound insulation in the low- and medium-frequency regions. From the point of view of the average energy input value, improperly assigned $g_{11}^{(5)}$ can also deteriorate the system's sound insulation in the high-frequency region. In this simulation, the significant effective sound insulation frequency range is about 1~400 Hz with proper assignment of $g_{11}^{(5)}$.

Combining Figure 6c–f, in the narrow region on the right side very close to $g_{11}^{(5)} = 0$, the first resonance peak is basically eliminated, which indicates that the sound insulation effect of the system is well. Outside this narrow region, the peak values are all significantly lower than at $g_{11}^{(5)} = 0$, indicating that the system also has some sound insulation effect. However, there is an elevated resonance peak in the local region on the left side very close to $g_{11}^{(5)} = 0$. This indicates that the $g_{11}^{(5)}$ at this time exacerbates the resonance effect and deteriorates the system's sound insulation.

In summary, the effective range of the feedback parameters for the relative velocity feedback control method is narrow. Within the effective range of values, it can improve the system's low- and medium-frequency sound insulation capability. However, outside the effective range, it does not play a role in the system's low- and medium-frequency sound insulation, and even plays a deteriorating role in the system's high-frequency sound insulation. On the whole, the sound insulation effect under the relative velocity feedback control method is worse than that of the absolute velocity feedback control method.

As shown in Figure 7a,b, the overall P_{tr} curve has a slight rightward shift as $\left|g_{11}^{(6)}\right|$ increases. Small fluctuations precede the first resonance peak in the low- and medium-frequency domains under the action of $g_{11}^{(6)}$. In the high-frequency region, $g_{11}^{(6)}$ does not make the problem solved, where the system's higher-order modes are excited and trigger a large number of peaks, and even the P_{tr} value increases slightly. From the point of view of resonant frequencies, improperly assigned $g_{11}^{(6)}$ can slightly deteriorate the system's sound insulation in the low- and medium-frequency regions. From the point of view of the average energy input value, improperly assigned $g_{11}^{(6)}$ can also deteriorate the system's sound insulation in the high-frequency region. In this simulation, the significant effective sound insulation frequency range is about 1~400 Hz with proper assignment of $g_{11}^{(6)}$.

Combining Figure 7c–f, in the narrow region on the right side very close to $g_{11}^{(6)} = 0$, the first resonance peak is basically eliminated, which indicates that the sound insulation effect of the system is well. Outside this narrow region, although the peak is reduced compared to that at $g_{11}^{(6)} = 0$, it is not very significant. In addition to the first resonance peak, the second and third resonance peaks are still present. Some values of $g_{11}^{(6)}$ cause a fluctuation in the frequency domain before the first resonance peak of the system. This indicates that the system's sound insulation deteriorates at this time.

In summary, the effective range of the feedback parameters for the relative acceleration feedback control method is narrow. Within the effective range of values, it can improve the system's low- and medium-frequency sound insulation capability. However, outside the effective range, it does not play a role in the system's low- and medium-frequency sound insulation, and even plays a deteriorating role in the system's low-, medium-, and high-frequency sound insulation. On the whole, the sound insulation effect under the relative acceleration feedback control method is worse than that of the absolute acceleration feedback control method.

4. Conclusions and Outlook

4.1. Conclusions

In this paper, active feedback control is used to solve the low-frequency sound insulation problem of the double-layer plate system. Based on the theoretical model of the coupling system of the elastic plate structure and water-filled acoustic cavity, a four-terminal parameters transfer matrix is introduced to achieve active feedback control. The theoretical model of the sound insulation system with a double-layer plate structure and active feedback control strategy is established for the water-filled acoustic cavity. The average energy input is taken as the evaluation index of the active sound insulation effect of the system, and its calculation method is derived. The effect of different feedback parameters on the average energy transfer characteristics is analyzed by MATLAB numerical calculations using an active sound insulation system of a double-layer plate with four supports as an example. The following conclusions are drawn.

(1) Based on the proper assignment of feedback parameters, the six feedback control methods of absolute displacement, velocity, and acceleration and relative displacement, velocity, and acceleration can all produce significant effects on the low-frequency sound insulation of the system, and can achieve controllable peak shaving and frequency reduction of the resonance peaks.

(2) Among these six feedback parameter control methods, only the absolute acceleration feedback control method has a more obvious effect on the high-frequency sound insulation of the system, while the other feedback control methods are not beneficial or even harmful to that.

(3) Among these six feedback parameter control methods, the amplitude-frequency response of average energy input in the system with the absolute acceleration feedback control method is the most sensitive.

(4) The overall sound insulation effect under the absolute displacement, velocity, and acceleration feedback parameter control methods is better than that under the relative displacement, velocity, and acceleration feedback parameter control methods.

4.2. Outlook

In this paper, only the sound insulation effect of the system is researched when each feedback parameter acts alone. However, in the face of active control systems with different research purposes or design requirements, the joint control of multiple feedback parameters is inevitably used. Therefore, it is also necessary to analyze the sound insulation of the system under the joint control mode of multiple feedback parameters. However, there are $C_6^2 + C_6^3 + C_6^4 + C_6^5 + C_6^6 = 57$ ways to combine two or more feedback parameters together. Due to the limited time and space, the research on the system's sound insulation problem under the joint control mode of multiple feedback parameters is not carried out further in this paper, and will continue to be studied in-depth in the future.

References

1. Wan, L.L.; Wang, X.P.; Chen, T.N.; Wang, F.; Du, X.W.; Zhang, Z.H. Acoustic super-surface for low frequency sound insulation. In Proceedings of the 27th National Conference on Vibration and Noise Applications, Harbin, China, 27 July 2016.
2. Liang, B.N. Vibration and Acoustic Performance Study of Floating Compartments of Ships. Ph.D. Thesis, Dalian Maritime University, Dalian, China, 2016.
3. Yucel, A.; Arpaci, A.; Degirmenci, S.; Tuzdengi, T. A new foundation design approach as a vibration reducer for marine gensets. *Ships Offshore Struct.* **2020**, *15*, 89–98. [CrossRef]
4. La, V.D. A Simple Frequency Range Selector to Reduce the Unstable Behavior of Active Vibration Isolation. *J. Dyn. Syst. Meas. Control* **2020**, *142*, 114502–114508. [CrossRef]
5. Yu, M.S.; Lin, L. Thirty years of basic progress and some frontier basic problems in underwater noise research of ships. *J. Ship. Mech.* **2017**, *21*, 244–248.
6. Yan, G.; Wang, S.; Zou, H.X.; Zhao, L.C.; Gao, Q.H.; Zhang, W.M. Bio-inspired polygonal skeleton structure for vibration isolation: Design, modelling, and experiment. *Sci. China Technol. Sci.* **2020**, *63*, 2617–2630. [CrossRef]
7. Yi, Q.; Li, C.L. Research status and development trend of active control technology of mechanical vibration. *Mech. Eng. Aut.* **2016**, 220–221. [CrossRef]
8. Liu, J.; Li, C.F. Active soundproof earmuffs system with passive sound insulation structure compensation. *Appl. Acoust* **2020**, *165*, 107321. [CrossRef]

9.   Tang, Y.; Wang, X.; Li, H.; Gao, C.; Miao, X.H. Experimental research on interior field noise and the vibration characteristics of composite reinforced sheet-beam structures. *Appl. Acoust.* **2020**, *160*, 107154. [CrossRef]

10.   Wang, J.W. Vibroacoustic Simulation of Carbon Fiber Composite Plates and Its Parameter Influence Characteristics. Master's Thesis, Shandong University, Jinan, China, 2019.

11.   Xu, B.B.; Wang, D.Y.; Wu, H.L.; Zhu, X.J.; Cui, S.M. Predictive Design Techniques for Sound Insulation Characteristics of Sound Insulation Devices. *Chin. J. Constr. Mach.* **2015**, 376–380. [CrossRef]

12.   Gao, S. Study of Acoustic Vibration Characteristics of Typical Reinforced Plate Structures of Ships. Master's Thesis, Huazhong University of Science and Technology, Wuhan, China, 2017.

13.   Kaidouchi, H.; Kebdani, S.; Slimane, S.A. Vibro-acoustic analysis of the sound transmission through aerospace composite structures. *Mech. Adv. Mater. Struct.* **2022**, 1–11. [CrossRef]

14.   Yang, H.S. Study of Vibro-Acoustic Properties of Corrugated Core Sandwich Plate Considering Acoustic-Solid Coupling. Ph.D. Thesis, Shanghai Jiao Tong University, Shanghai, China, 2017.

15.   Gao, Y.; Jiang, W.A.; Liu, K.; Wang, J.X.; Wang, Z.L. Folded sandwich plate lightweight design and vibration damping, sound insulation and noise reduction performance analysis. In Proceedings of the 2019 Ship Structural Mechanics Conference, Wuhan, China, 22 August 2019.

16.   Langfeldt, F.; Hoppen, H.; Gleine, W. Broadband low frequency sound transmission loss improvement of double walls with Helmholtz resonators. *J. Sound Vib.* **2020**, *476*, 115309. [CrossRef]

17.   Leng, C.L. Simulation analysis of double-layer plate sound insulation volume. In Proceedings of the 2019 Academic Conference of the Hydroacoustics Branch of the Chinese Society of Acoustics, Nanjing, China, 25 May 2019.

18.   Bai, Z.G. Double-Layer Cylindrical Shell Outboard Acoustic Vibration Coupling Characteristics and Control Technology. Ph.D. Thesis, China Ship Research and Development Academy, Beijing, China, 2014.

19.   Zhang, Z.; Wang, J.; Li, Z.; Zhang, X.R. Broadband Sound Insulation and Dual Equivalent Negative Properties of Acoustic Metamaterial with Distributed Piezoelectric Resonators. *Materials* **2022**, *15*, 4907. [CrossRef] [PubMed]

20.   Lv, H.; Zhang, S.; Sun, Q.; Chen, R.; Zhang, W.J. The dynamic models, control strategies and applications for magnetorheological damping systems: A systematic review. *J. Vib. Eng. Technol.* **2021**, *9*, 131–147. [CrossRef]

21.   Zhou, W.; Li, D.X. Design and analysis of an intelligent vibration isolation platform for reaction/momentum wheel assemblies. *J. Sound Vib.* **2012**, *331*, 2984–3005. [CrossRef]

22.   Ahmed, M.R.; Yusoff, A.R.; Romlay, F.R.M. Numerical Investigation of Continuous Damping of The Semi-Active Suspension System for Passenger Car. *Mater. Sci. Eng.* **2019**, *530*, 012014. [CrossRef]

23.   Ma, X.; Chen, K.; Xu, J. Active control of sound transmission through orthogonally rib stiffened double-panel structure: Mechanism analysis. *Appl. Sci.* **2019**, *9*, 3286. [CrossRef]

24.   Zuo, X.L.; Su, J.C.; Wang, Z.H. Simulation study of feedback-controlled vibration isolation performance of double-layer vibration isolation system. *J. Eng. Therm. Energ. Power* **2018**, *33*, 44–49.

25.   Du, X.; Yu, M.; Fu, J.; Huang, C.Q. Experimental study on shock control of a vehicle semi-active suspension with magneto-rheological damper. *Smart Mater. Struct.* **2020**, *29*, 074002. [CrossRef]

26.   Zeng, Y.C.; Zhang, W.H.; Song, D.L. Lateral-vertical coupled active suspension on railway vehicle and optimal control methods. *Veh. Syst. Dyn.* **2022**, *60*, 258–280. [CrossRef]

27.   Loghmani, A.; Danesh, M.; Kwak, M.K.; Keshmiri, M. Active control of radiated sound power of a smart cylindrical shell based on radiation modes. *Appl. Acoust.* **2016**, *114*, 218–229. [CrossRef]

28.   Du, G.H.; Zhu, Z.M.; Gong, X.F. *Fundamentals of Acoustics*, 3rd ed.; Nanjing University Publisher: Nanjing, China, 2012; pp. 126–127.

29.   Huo, R.; Li, C.Y.; Jing, L.Z.; Wang, W.K. Research On power flow transmission through elastic structure into a fluid-filled enclosure. *Adv. Acoust. Vib.* 2018. [CrossRef]